View metadata, citation and similar papers at core.ac.uk

brought to you by CORE

provided by CERN Document Server

arXiv:astro-ph/0606096 v1 5 Jun 2006

Accepted to Astrophysical Journal

A *Spitzer*[1] Infrared Radius for the Transiting Extrasolar Planet HD 209458 b

L. Jeremy Richardson

Exoplanets and Stellar Astrophysics Laboratory, NASA's Goddard Space Flight Center, Mail Code 667, Greenbelt, MD 20771

richardsonlj@milkyway.gsfc.nasa.gov

Joseph Harrington

Center for Radiophysics and Space Research, Cornell Universtiy, 326 Space Sciences Bldg., Ithaca, NY 14853-6801

jh@oobleck.astro.cornell.edu

Sara Seager

Department of Terrestrial Magnetism, Carnegie Institution of Washington, 5241 Broad Branch Rd NW, Washington, DC 20015

seager@dtm.ciw.edu

Drake Deming

Planetary Systems Laboratory, NASA's Goddard Space Flight Center, Mail Code 693, Greenbelt, MD 20771

ddeming@pop600.gsfc.nasa.gov

ABSTRACT

We have measured the infrared transit of the extrasolar planet HD 209458 b using the Spitzer Space Telescope. We observed two primary eclipse events (one partial and one complete transit) using the 24 μm array of the Multiband Imaging Photometer for Spitzer (MIPS). We analyzed a total of 2392 individual images (10-second integrations) of the planetary system, recorded before, during, and after transit. We perform optimal photometry on the images and use the local

zodiacal light as a short-term flux reference. At this long wavelength, the transit curve has a simple box-like shape, allowing robust solutions for the stellar and planetary radii independent of stellar limb darkening, which is negligible at 24 μm. We derive a stellar radius of $R_* = 1.06 \pm 0.07$ $R_\odot$, a planetary radius of $R_p = 1.26 \pm 0.08$ R_J, and a stellar mass of 1.17 $M_\odot$. Within the errors, our results agree with the measurements at visible wavelengths. The 24 μm radius of the planet therefore does not differ significantly compared to the visible result. We point out the potential for deriving extrasolar transiting planet radii to high accuracy using transit photometry at slightly shorter IR wavelengths where greater photometric precision is possible.

Subject headings: extrasolar planets, stars: individual (HD 209458)

1. Introduction

The transit of an extrasolar planet across its star allows us to measure the radius of the planet (Charbonneau et al. 2000; Henry et al. 2000; Brown et al. 2001). Of the ten known transiting planets, HD 209458 b, with a radius (at visible wavelengths) of 1.320 ± 0.025 R_J (Knutson et al. 2006), is inflated compared to the other known transiting planets and thus has a lower bulk density. One explanation for the anomalous radius was inflation by the dissipation of tidal stress within the planet (Bodenheimer et al. 2001). However, the timing of the secondary eclipse as observed by the Spitzer Space Telescope (Deming et al. 2005b), as well as improved radial velocity observations (Laughlin et al. 2005), have ruled out a non-zero orbital eccentricity of the magnitude ($\sim$0.03) needed by the tidal dissipation theory. Showman & Guillot (2002) suggest that kinetic energy produced by atmospheric circulation and deposited in the planet's interior could account for the missing energy source and increase the planetary radius. Another popular proposed explanation is the possibility of obliquity tides (Winn & Holman 2005), in which a non-zero obliquity (made possible by a spin-orbit resonance) could drive the tidal dissipation and provide the necessary energy to give the planet an inflated radius.

Our Spitzer program to measure the 24 μm flux of HD 209458 b includes observations during transit (i.e., primary eclipse), revealing the infrared (IR) radius of the planet, which

[1]This work is based on observations made with the Spitzer Space Telescope, which is operated by the Jet Propulsion Laboratory, California Institute of Technology under a contract with NASA. Support for this work was provided by NASA.

is reported in this paper. Section 2 further elaborates on why an IR radius measurement is of interest. Section 3 describes the observations; section 4 explains the photometric data analysis and radius fit. Section 5 concludes with results and discussion.

2. Motivation for Infrared Radius Measurements

The reduced stellar flux at mid-IR wavelengths implies that transit photometry in this region is unable to achieve the high photometric precision obtained at visible wavelengths (Brown et al. 2001). However, stellar limb darkening weakens with increasing wavelength due to the increasing H^- free-free opacity (Vernazza et al. 1976). Thus, the fitting of transit curves to mid-IR data is simple and robust, and gives results independent of limb-darkening parameterizations. A mid-IR radius measurement is also of intrinsic interest for understanding the planet. Observations of the planet during transit suggest that clouds and scattering layers could potentially extend to great heights. The low sodium abundance reported by Charbonneau et al. (2002) and the upper limit on CO reported by Deming et al. (2005a) both support this physical picture of the planet's atmosphere. Furthermore, the escaping atmosphere observed by Vidal-Madjar et al. (2003) suggests that other processes may be at work in planet's atmosphere. The scale height of the atmosphere is $\sim$450 km, and if the clouds extend to even a few scale heights, this would represent $\sim$0.01 R_J. While our observations are not able to reach that level of precision in the planetary radius, it is nonetheless valuable to search for unexpectedly large variations in the planetary radius as a function of wavelength. A major goal of our observational program was to test this scenario by measuring the 24 μm radius of HD 209458 b.

3. Observations

We observed two transit events using the Spitzer Space Telescope (Werner et al. 2004): a half eclipse event (ingress only) on 2004 December 5 and a full eclipse event on 2005 June 27. We used the MIPS (Rieke et al. 2004) 24 μm array, which is a Si:As detector with 128$\times$128 pixels and an image scale of 2.55 arcsec pixel^{-1}. We obtained two series of 10-second exposures using the standard MIPS raster pattern, which places the star at 14 different positions on the array. This produced 864 images during the half eclipse event and 1728 images during the full eclipse event.

4. Analysis

4.1. Photometry

We first reject obviously bad images, including those with strong 'jailbar' features[2], as well as the initial image of each cycle due to a prominent 'first frame' effect. This leaves 780 images for the half eclipse event, and 1612 images for the full eclipse event. We analyze each eclipse event separately. For each of the 14 raster positions, we perform the following steps:

1. *Median filter the images to remove energetic particle events and hot pixels.* The median image is computed from all the images (typically 60) at a given raster position, and the difference image is constructed by subtracting the median image from a given image. We then employ a routine called SIGMA_FILTER[3], which computes the mean and standard deviation of the pixels within a box of specified width (excluding the center pixel). If the center pixel is deviant by more than a specified number of standard deviations from its neighbors, it is replaced by the mean of the remaining pixels in the box. We use a box width of 20 pixels and a sigma limit of 10, and iterate until no more pixels are changed. This cleans most of the hot pixels evident in a given image. Rejected from further consideration are any images in which a pixel within the defined aperture containing the star is changed.

2. *Calculate and subtract the total zodiacal background from all pixels in a given image.* The background level for each image is determined by constructing a histogram of all pixels in an image (with a bin size of 0.01 MJy/sr) and fitting a Gaussian to the histogram. The center of the Gaussian fit is then the 'average' background level for that image, and this constant level is subtracted from the each pixel in the image to create the background-subtracted image.

3. *Find the center of the star to a precision of 0.01 pixel by dithering the theoretical point spread function (PSF) over the individual images and finding the best fit.* The theoretical PSF was obtained[4] for a 5000 K blackbody on the center of the 24 μm array. These files have been modeled using Tiny Tim (Krist 1993). We first resample the theoretical PSF to a scale 100 times finer for comparison to the real data. The resampled PSF is dithered in both dimensions, and the 'best-fit' PSF to the data (using linear least squares) determines the center of the star.

---

[2]See the MIPS Data Handbook, available at `http://ssc.spitzer.caltech.edu/mips/dh/`

[3]See the IDL Astronomy Library at `http://idlastro.gsfc.nasa.gov/contents.html`

[4]See `http://ssc.spitzer.caltech.edu/mips/psffits/` and the file `mips_24_5000c.fits`.

4. *Use the best-fit PSF to weight the pixels near the star before adding them.* This is applied to the background-subtracted images and produces optimal photometry (analogous to Horne 1986). The errors are derived by propagating the MIPS errors through the optimal error formula (Horne 1986, see his Table 1, item 8). The errors are dominated by statistical fluctuations in the zodiacal background. The optimal photometry typically provides a S/N improvement of 50% or more over the standard aperture photometry approach (where the pixels are summed with no weighting function).

5. *Normalize the optimal photometry to the total background level in the frame.* The total background level is simply the average of all the points (except those in a 3×3 box surrounding the star) in a given image. This gives the stellar intensity relative to the zodi and thus removes any remaining instrument response variations.

Having completed these steps for each raster position, we recombine the data to obtain the entire time series for each eclipse event. Time is converted to orbital phase using the most recent and most accurate orbital period and ephemeris (Knutson et al. 2006), and we account for the light travel time between the Sun and Spitzer. The zodiacal background changes linearly by ∼1.5% over the six-hour duration over which the full eclipse event is observed, and we remove this effect from both eclipses separately. We estimated the magnitude of this change using the Spitzer Observations Planning Tool (SPOT), which employs the zodiacal dust model from Kelsall et al. (1998). Finally, the time series are normalized to an average of unity for the out-of-transit points.

The calibrated, unbinned photometry is given in Table 1 and is shown in Figure 1 (upper panel). The upper panel shows the aggregate data for both events combined (2392 points), and it clearly reveals the eclipse. The lower panel shows the average in bins of phase width 0.001; the box-like shape of the light curve due to the lack of stellar limb darkening is quite evident. To perform the optimal photometry, we used two independent codes, derived from the same basic algorithm but constructed by individual researchers. We obtained virtually identical per-point results with both.

4.2. Light Curve Fitting

We construct a family of simple, approximate light curves by connecting intensities at the contact times with straight line segments. Four observable parameters uniquely describe a light curve in the absence of stellar limb darkening: 1) the duration of full eclipse (i.e., the time between second and third contact, $t_{\rm F}$), 2) the total duration of the eclipse (i.e., the time between first and fourth contact, $t_{\rm T}$), 3) the eclipse depth, and 4) the observed

time of center eclipse. We derive best-fit values for these four observables by minimizing the reduced chi-squared (χ^2_ν) of the fits to each simple transit curve generated. We refer to this 'trial-and-error' technique as 'Method 1.' We have chosen a large enough range of parameters and small enough grid spacing to avoid finding only a local minimum. Figure 2 shows χ^2_ν as a function of $t_{\rm F}$ and $t_{\rm T}$ for zero phase offset (the best-fit value); the upper panel shows the contour plot for the χ^2_ν, and the lower panel casts the result in terms of confidence intervals. (The contours and confidence intervals are correctly calculated by projecting the χ^2_ν into the plane of interest; see Press et al. (1992, Section 15.6 and Figure 15.6.4).) The best-fit observables ($t_{\rm T}$, $t_{\rm F}$, eclipse depth, and time offset) are listed in Table 2 (column marked 'Method 1').

In order to verify the results from Method 1 and to ensure that we did not hit a local minimum, we employed a second method of finding the best-fit observables to the data, the MPFIT package[5], which performs a Levenberg-Marquardt least-squares fit. Combined with our own function that computes a theoretical eclipse (as described above), this method independently calculates the four observables, and these results are also shown in Table 2 (column marked 'Method 2'). We note that the two results agree closely, and we adopt the results from MPFIT (Method 2) as our formal results. Although the resulting minimum χ^2_ν is slightly larger, we nonetheless adopt Method 2 because it is computationally more efficient for calculating the errors on the individual parameters, as discussed below.

Using the analytic formulation of Seager & Mallén-Ornelas (2003), we derive the physical parameters of the system from the observables ($t_{\rm T}$, $t_{\rm F}$, and eclipse depth, obtained from the best-fit simple light curve, and the known orbital period (Knutson et al. 2006)). The impact parameter b, the ratio of the semi-major axis to the stellar radius, a/R_*, the orbital inclination i, and the stellar density ρ_* are derived immediately from these observables (Seager & Mallén-Ornelas 2003, see their Equations 7, 17–19)[6].

Determining the stellar and planetary radii from these parameters requires an assumption of the stellar mass (Brown et al. 2001). We assumed stellar masses between 0.9 and 1.30 $M_\odot$ (shown in Figure 3), covering a region surrounding the reported stellar mass of 1.146 $M_\odot$ (Brown et al. 2001). Interestingly, by using the analytic formulation, we note that the orbital inclination is determined by the transit times and the *ratio* of the stellar radius to the orbital semi-major axis; this means that our assumption of the stellar mass, while determining the stellar radius, does not affect the orbital inclination.

---

[5]`http://cow.physics.wisc.edu/~craigm/idl/idl.html`

[6]Note that their Equation 19, derived from Equation 9, is missing a factor of $\frac{4}{3}\pi$.

We use a bootstrap Monte Carlo method (Press et al. 1992, see Section 15.6) to determine realistic errors in the observables and physical parameters. We randomly select N=2392 data points with replacement (meaning some points are duplicated) to create a 'synthetic' data set. We create 10000 such synthetic data sets, perform the same fitting procedure described above (again, Method 2, using MPFIT) to each one, and derive the physical parameters from the best-fit observables. In this way, we derive a set of physical parameters (R_*, R_p, and i) for each of the 10000 synthetic data sets. Using the routine HISTOGAUSS (from the IDL Astronomy Library[7]), we fit a Gaussian to each one of the arrays of observables and physical parameters. All parameters are normally distributed and symmetric, so that the width of each best-fit Gaussian represents the 1-σ error in the associated parameter, and these are the uncertainties presented in Tables 2 and 3.

The bootstrap method was also performed on each of the eclipse events separately to determine the observed time of center eclipse, as shown in Table 4. Both are consistent with zero offset in time from the predicted value. For the half eclipse (event 1), we set the full eclipse time (t_F) to the value derived from fitting the aggregate data and hold it fixed, while minimizing the other three observables. As expected, the uncertainty in the time of center for the half eclipse is much larger than that of the full eclipse.

Next, we check the radii and orbital inclination by removing the approximation that the light curve is comprised of straight line segments. We have developed a routine to compute light curves numerically (Richardson et al. 2006), and we include the small effect due to predicted limb darkening at 24 μm, derived from a Kurucz[8] model atmosphere for stellar parameters $T_e = 6000$ K, $\log g = 4.5$, and [Fe/H]= 0.0. We validated the code by verifying that we can reproduce the fits to the very precise HST optical data from Brown et al. (2001). We adopted the derived parameters from the best-fit simple curve and calculated an exact theoretical light curve. The result is plotted as a dashed line in the lower panel of Figure 1, but it is hard to see since it is nearly identical to the simple curve. The χ^2_ν of the fits for each of the two curves to the data are nearly identical: 1.0060 for the best-fit simple curve from MPFIT, compared to 1.0061 for the theoretical light curve. We therefore conclude that the limb darkening is negligible at 24 μm (as expected) and that the simple light curve composed of straight line segments is an accurate method of deriving the physical parameters.

Finally, we checked our results by incorporating information from the transit at visible wavelengths (Brown et al. 2001). There the transit depth is 0.0164, compared to $0.0149 \pm$

[7]`http://idlastro.gsfc.nasa.gov/contents.html`

[8]Available from http://kurucz.harvard.edu. We linearly interpolate the Kurucz parameters at 20 and 40 μm to estimate the values at 24 μm.

0.0003 at 24 μm, a significant difference. The ratio of visible to IR transit depth can be used to determine the impact parameter, the minimum projected radius where at which the planet crosses the star, and thereby the orbital inclination. That is, we are deriving the degree of limb darkening at the given projected stellar radius of closest approach and using the Kurucz model to determine the location of the chord. We used the limb darkening tabulated by a Kurucz model atmosphere (same parameters used above), and the 'small planet' approximation from Mandel & Agol (2002). We calculated numerically the ratio of visible to IR transit depth as a function of impact parameter. Comparing the observed ratio (1.100±0.03) to this relation gives an impact parameter of 0.58±0.07, and an orbit inclination of $86.6^\circ \pm 0.6^\circ$. Within the errors, this agrees with the results at visible wavelengths (Brown et al. 2001; Wittenmyer et al. 2005) and is consistent with the $i = 87.97^\circ \pm 0.85^\circ$ value we derive internally from our IR data. This calculation serves as an independent check of our results and a direct comparison to the visible results.

5. Results and Discussion

We have computed the stellar density directly from the observable quantities from the best-fit simple curve (Seager & Mallén-Ornelas 2003). Assuming a stellar mass allows us to calculate the stellar radius. This empirical mass-radius relation is shown in Figure 3, where we have derived the radii for stellar masses from 0.9 to 1.3 $M_\odot$. We break the degeneracy by intersecting the stellar radius curve with the mass-radius relation from Cody & Sasselov (2002), which is derived by fitting stellar models to a constant luminosity. This is shown as the dashed line in Figure 3, following Wittenmyer et al. (2005, their Figure 5). On this basis, we derive the stellar mass to be $M = 1.171\ M_\odot$, with $R_* = 1.06 \pm 0.07\ R_\odot$ and $R_p = 1.26 \pm 0.08\ R_J$. Our result for the planetary radius agrees with the updated visible radius of $R_p = 1.320 \pm 0.025\ R_J$ (Knutson et al. 2006).

We are encouraged by the fact that our radius error is only four times larger than that obtained by Knutson et al. (2006), in spite of the fact that our infrared photometric precision is an order of magnitude poorer than the HST visible photometry. We attribute this to the character of the IR transit curve, where the lack of limb darkening produces a simple transit shape, from which radius information can be extracted with maximum efficiency. We point out that photometry at other accessible Spitzer wavelengths such as 8 and 16 μm would provide much higher photometric precision for bright transiting systems, because the stellar flux will be much higher, and the zodiacal background will not be a limiting factor. Limb darkening remains sufficiently weak at these shorter IR wavelengths to maintain a relatively simple transit light curve shape. Considering also that Spitzer's heliocentric orbit allows

uninterrupted observations of complete transits, we suggest that IR transit photometry from Spitzer may be the optimal method for precise radius determination in bright transiting planet systems.

This work is based on observations made with the Spitzer Space Telescope, which is operated by the Jet Propulsion Laboratory, California Institute of Technology under a contract with NASA. Support for this work was provided by NASA. LJR acknowledges support as a NASA Postdoctoral Fellow (formerly NRC Research Associate) at NASA Goddard. We thank the referee for insightful comments and suggestions that significantly improved the manuscript.

Facilities: Spitzer(MIPS)

REFERENCES

Bodenheimer, P., Lin, D. N. C., & Mardling, R. A. 2001, ApJ, 548, 466

Brown, T. M., Charbonneau, D., Gilliland, R. L., Noyes, R. W., & Burrows, A. 2001, ApJ, 552, 699

Charbonneau, D., Brown, T. M., Latham, D. W., & Mayor, M. 2000, ApJ, 529, L45

Charbonneau, D., Brown, T. M., Noyes, R. W., & Gilliland, R. L. 2002, ApJ, 568, 377

Cody, A. M. & Sasselov, D. D. 2002, ApJ, 569, 451

Deming, D., Brown, T. M., Charbonneau, D., Harrington, J., & Richardson, L. J. 2005a, ApJ, 622, 1149

Deming, D., Seager, S., Richardson, L. J., & Harrington, J. 2005b, Nature, 434, 740

Henry, G. W., Marcy, G. W., Butler, R. P., & Vogt, S. S. 2000, ApJ, 529, L41

Horne, K. 1986, PASP, 98, 609

Kelsall, T., Weiland, J. L., Franz, B. A., Reach, W. T., Arendt, R. G., Dwek, E., Freudenreich, H. T., Hauser, M. G., Moseley, S. H., Odegard, N. P., Silverberg, R. F., & Wright, E. L. 1998, ApJ, 508, 44

Knutson, H., Charbonneau, D., Noyes, R. W., Brown, T. M., & Gilliland, R. L. 2006, ArXiv Astrophysics e-prints

Krist, J. 1993, in ASP Conf. Ser. 52: Astronomical Data Analysis Software and Systems II, ed. R. J. Hanisch, R. J. V. Brissenden, & J. Barnes, 536–+

Laughlin, G., Wolf, A., Vanmunster, T., Bodenheimer, P., Fischer, D., Marcy, G., Butler, P., & Vogt, S. 2005, ApJ, 621, 1072

Mandel, K. & Agol, E. 2002, ApJ, 580, L171

Press, W. H., Teukolsky, S. A., Vetterling, W. T., & Flannery, B. P. 1992, Numerical Recipes in C: The Art of Scientific Computing, 2nd edn. (Cambridge University Press)

Richardson, L. J., Seager, S., Deming, D., Harrington, J., Barry, R. K., Rajagopal, J., & Danchi, W. C. 2006, in IAUC 200, Direct Detection of Exoplanets: Science and Techniques, in press, ed. C. Aime & F. Vakili

Rieke, G. H., Young, E. T., Engelbracht, C. W., Kelly, D. M., Low, F. J., Haller, E. E., Beeman, J. W., Gordon, K. D., Stansberry, J. A., Misselt, K. A., Cadien, J., Morrison, J. E., Rivlis, G., Latter, W. B., Noriega-Crespo, A., Padgett, D. L., Stapelfeldt, K. R., Hines, D. C., Egami, E., Muzerolle, J., Alonso-Herrero, A., Blaylock, M., Dole, H., Hinz, J. L., Le Floc'h, E., Papovich, C., Pérez-González, P. G., Smith, P. S., Su, K. Y. L., Bennett, L., Frayer, D. T., Henderson, D., Lu, N., Masci, F., Pesenson, M., Rebull, L., Rho, J., Keene, J., Stolovy, S., Wachter, S., Wheaton, W., Werner, M. W., & Richards, P. L. 2004, ApJS, 154, 25

Seager, S. & Mallén-Ornelas, G. 2003, ApJ, 585, 1038

Showman, A. P. & Guillot, T. 2002, A&A, 385, 166

Vernazza, J. E., Avrett, E. H., & Loeser, R. 1976, ApJS, 30, 1

Vidal-Madjar, A., des Etangs, A. L., Désert, J.-M., Ballester, G. E., Ferlet, R., Hébrard, G., & Mayor, M. 2003, Nature, 422, 143

Werner, M. W., Roellig, T. L., Low, F. J., Rieke, G. H., Rieke, M., Hoffmann, W. F., Young, E., Houck, J. R., Brandl, B., Fazio, G. G., Hora, J. L., Gehrz, R. D., Helou, G., Soifer, B. T., Stauffer, J., Keene, J., Eisenhardt, P., Gallagher, D., Gautier, T. N., Irace, W., Lawrence, C. R., Simmons, L., Van Cleve, J. E., Jura, M., Wright, E. L., & Cruikshank, D. P. 2004, ApJS, 154, 1

Winn, J. N. & Holman, M. J. 2005, ApJ, 628, L159

Wittenmyer, R. A., Welsh, W. F., Orosz, J. A., Schultz, A. B., Kinzel, W., Kochte, M., Bruhweiler, F., Bennum, D., Henry, G. W., Marcy, G. W., Fischer, D. A., Butler, R. P., & Vogt, S. S. 2005, ApJ, 632, 1157

This preprint was prepared with the AAS LaTeX macros v5.2.

Table 1. Calibrated, unbinned photometry.

HJD	Phase	Relative Intensity	Error
2453344.6466211	-0.03728	1.009530	0.008265
2453344.6467485	-0.03724	1.001394	0.008643
2453344.6468759	-0.03721	1.010476	0.008172
2453344.6470034	-0.03717	1.012307	0.008398
2453344.6471308	-0.03713	0.992136	0.008321

[The complete version of this table is in the electronic edition of the Journal. The printed edition contains only a sample.]

Table 2. Observables derived from χ^2_ν minimization of simple eclipse curves.

Parameter	Method 1	Method 2	Error
Depth	0.01496	0.01493	0.00029
$t_{\rm T}$ (hr)	2.978	2.979	0.051
$t_{\rm F}$ (hr)	2.254	2.253	0.058
Time Offset (hr)	0.000	0.001	0.013
χ^2_ν	1.00514	1.00598	-

Table 3. Derived physical parameters for the two minimization techniques.

Parameter	Method 1	Method 2	Error
Assumed Stellar Mass ($M_\odot$)	1.173	1.171	-
Stellar Radius ($R_\odot$)	1.063	1.064	0.069
Planetary Radius (R_J)	1.265	1.265	0.085
Orbital Inclination (deg)	88.00	87.97	0.85

Table 4. Observed time of center eclipse.

	Time (HJD)	Error
Event 1 (Half)	2453344.768245	0.002608
Event 2 (Full)	2453549.201422	0.000617

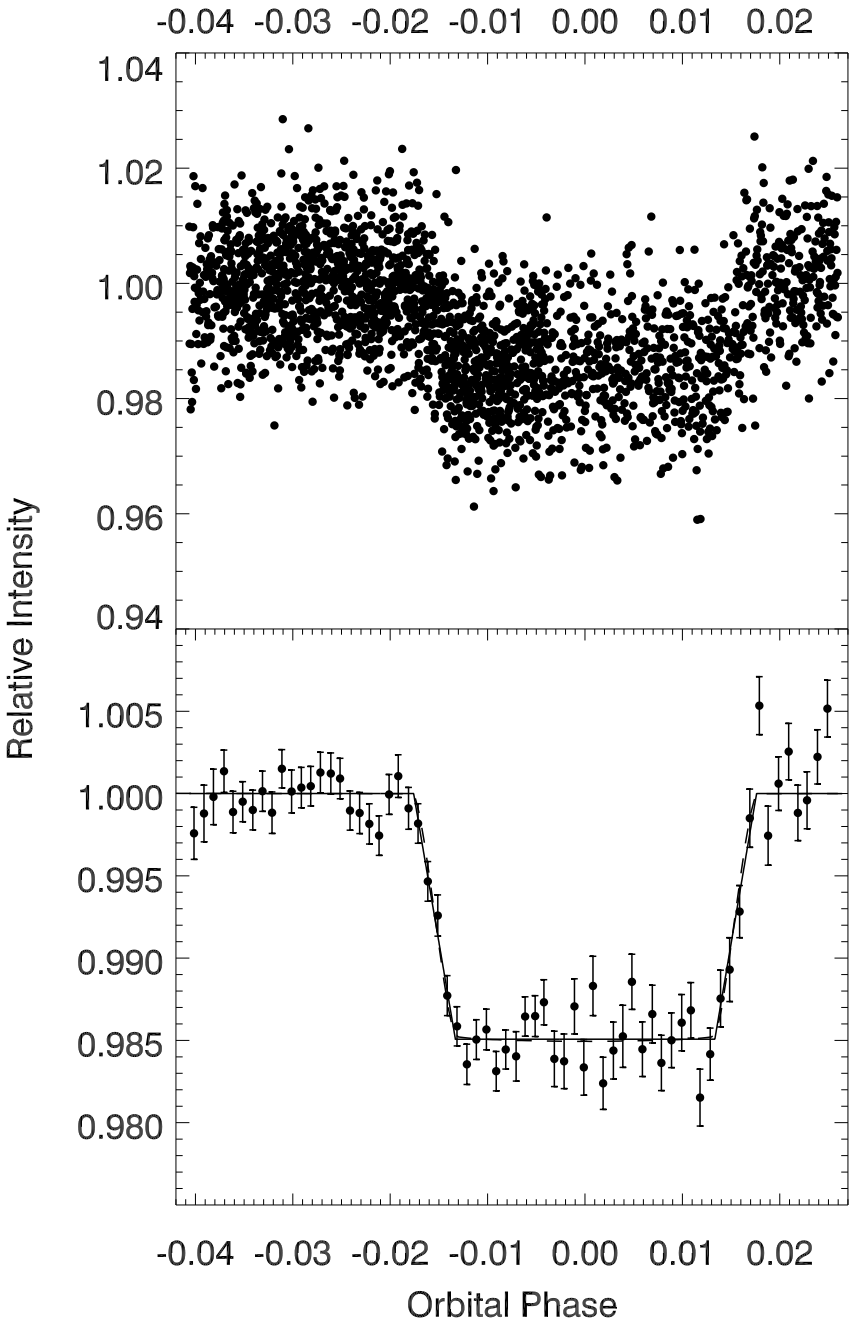

Fig. 1.— *Upper Panel:* All 2392 measurements versus heliocentric phase. *Lower Panel:* Data averaged in phase (bin size = 0.001 in phase); also shown are the best fit straight-line curve (solid line) and the exact theoretical light curve (dashed line, difficult to see), calculated using the best-fit physical parameters derived from the straight-line curve. Heliocentric phase was computed using the orbital period and ephemeris from Knutson et al. (2006).

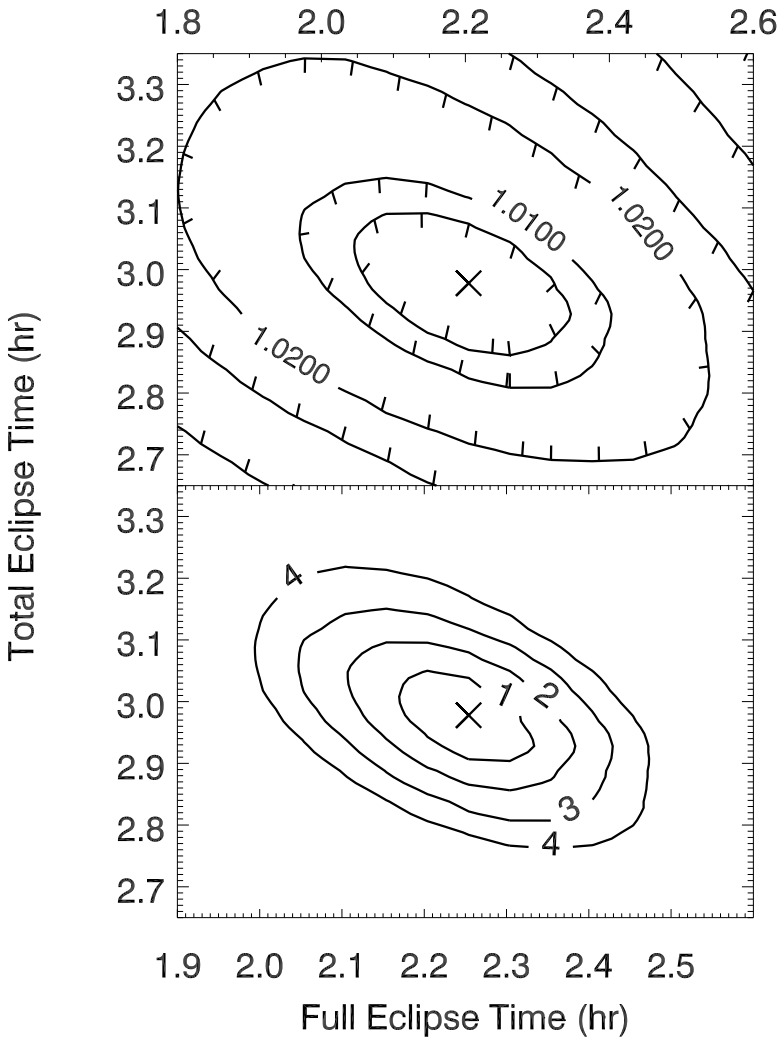

Fig. 2.— *Upper Panel:* Contour plot of the reduced chi-squared (χ^2_ν) fit from Method 1, showing the total eclipse time vs. the full eclipse time at zero phase offset (best-fit value). *Lower Panel:* Same result, but converted to confidence interval in standard deviations. In both panels, the minimum χ^2_ν (1.0051) is marked by an X.

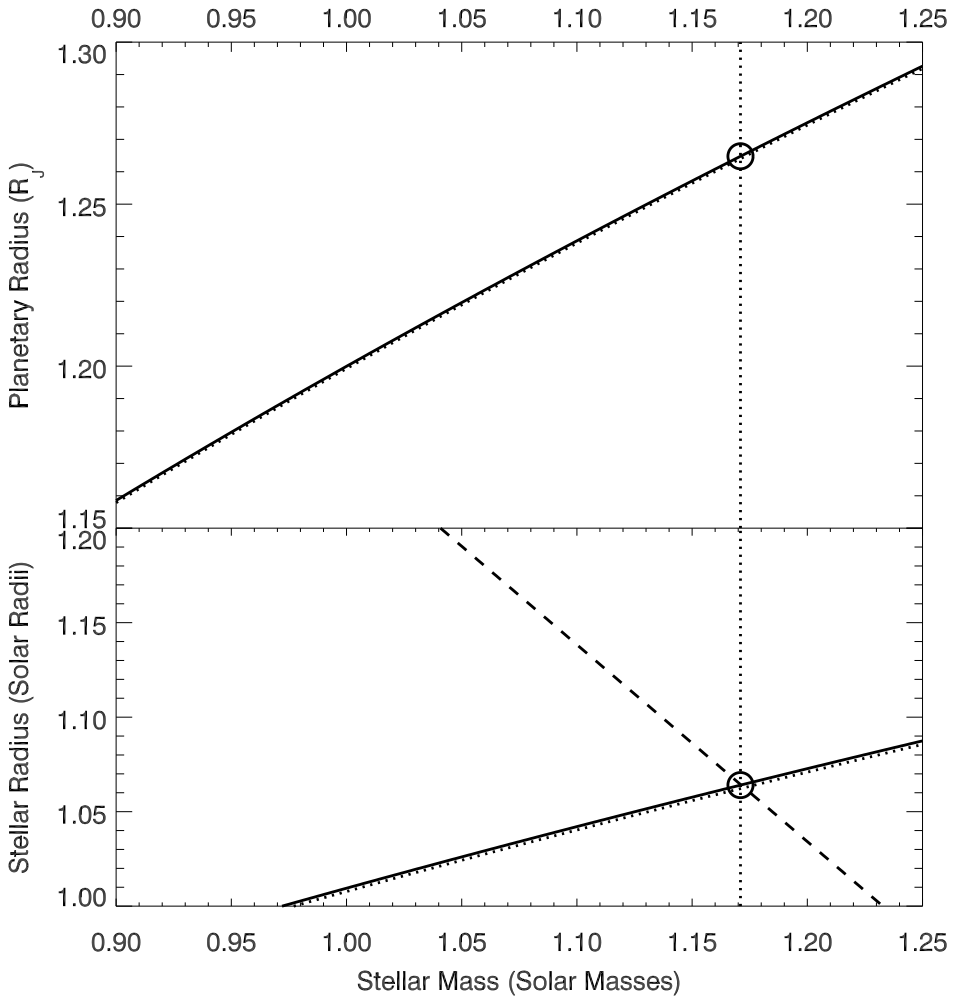

Fig. 3.— The stellar density derived from the best-fit parameters can be transformed to stellar radius by assumption of a range of stellar masses. The transit data therefore yield an empirical mass-radius relation. *Upper Panel:* Planetary radius as a function of assumed stellar mass. Solid line represents result from MPFIT (Method 2); dotted line represents the 'trial-and-error' minimization technique (Method 1). *Lower Panel:* Stellar radius as a function of assumed stellar mass. Methods 1 and 2 indicated as in upper panel. Dashed line represents mass-radius relation from Cody & Sasselov (2002). Intersection of this relation with the empirical curve to the assumed stellar masses allows a determination of the stellar mass (1.171 $M_{\odot}$), marked by the vertical dotted line. This reveals the best fit stellar and planetary radii, $R_* = 1.06\ R_{\odot}$ and $R_p = 1.26\ R_{\rm J}$.